communications biology

Article

https://doi.org/10.1038/s42003-024-07099-0

KLF13 promotes SLE pathogenesis by modifying chromatin accessibility of key proinflammatory cytokine genes

Andrew Wang[1,2], Anna-Marie Fairhurst[1,3], Kui Liu[1,4], Benjamin Wakeland[1], Spencer Barnes[5], Venkat S. Malladi[5], Kasthuribai Viswanathan[1], Carlos Arana[1], Igor Dozmorov[1], Amrita Singhar[1], Yong Du[6], Marjaan Imam[1], Angela Moses[1], Christian Chen[1], Ashwini Sunkavalli[1], Jose Casco[1], Dinesh Rakheja[7,8], Quan-Zhen Li[1,9], Chandra Mohan[6], Carol Clayberger[10], Edward K. Wakeland[1] & Shaheen Khan[1,8]

Although significant progress has been achieved in elucidating the genetic architecture of systemic lupus erythematosus (SLE), identifying genes underlying the pathogenesis has been challenging. The NZM2410-derived lupus susceptibility *Sle3 locus* is associated with T cell hyperactivity and activated myeloid cells. However, candidate genes associated with these phenotypes have not been identified. Here, we narrow the *Sle3* locus to a smaller genomic segment (*Sle3k*) and show that mice carrying *Sle3k* and *Sle1* loci developed lupus nephritis. We identify *Klf13* as the primary candidate gene that is associated with genome-wide transcription changes resulting in higher levels of proinflammatory cytokines, enhanced T cell activation, and hyperresponsiveness of myeloid cells. Correspondingly, *Klf13* $^{-/-}$ mice display repression of genes involved in mediating immune activation, including key proinflammatory cytokines/chemokines in T cells and dysregulation in cytokine signaling pathways in myeloid cells in response to toll receptor ligands. *Klf13* upregulation is associated with increased production of RANTES, a key chemokine in lupus nephritis, in activated T cells and the kidneys of lupus-prone mice. In sum, our findings reveal *Klf13* as a key gene in the *Sle3* interval in mediating lupus pathogenesis that may have implications in the rational design of new therapies for SLE.

Systemic lupus erythematosus (SLE) is a chronic multisystem autoimmune disease with extensive clinical heterogeneity, affecting mainly females. It is initiated with a breach in immune tolerance and characterized by the production of autoantibodies to a broad spectrum of self-antigens[1,2], leading to immune cell infiltrations of tissues, ultimately resulting in end-organ damage. Both genetic and environmental factors contribute to the complex immune dysregulation associated with the pathogenesis of SLE[3]. Genome-wide association studies (GWAS) in humans have identified more than 100 SLE risk loci[4–11], and numerous genes within these loci have been implicated in SLE. Murine lupus models have been key in elucidating the functional role of these genes toward SLE pathogenesis[12]. NZM2410, a recombinant inbred strain that resulted from an accidental backcross between NZB/W F1 and NZW, is widely used as a spontaneous lupus model. NZM2410 mice exhibit phenotypes similar to human SLE, including autoantibody production and lupus nephritis. Linkage analysis identified three NZM2410 susceptibility loci on chromosomes 1 (*Sle1*), 4 (*Sle2*), and 7 (*Sle3*) as being significantly correlated with the disease[13,14]. *Sle1* has been implicated in a breach in immune tolerance resulting in high levels of autoantibody production[15], and when combined with *Sle3*, the bicongenic *Sle1Sle3* mice developed severe lupus nephritis with high penetrance[16,17]. Previous studies have demonstrated that the *Sle3* locus contains at least two loci, *Sle3a*, and *Sle3b*, that independently interact with *Sle1* to mediate the transition to severe disease. Liu and colleagues identified kallikreins genes within the *Sle3b* interval as the disease-associated genes in anti-GBM

[1]Department of Immunology, The University of Texas Southwestern Medical Center, Dallas, TX, USA. [2]Department of Immunobiology, Yale School of Medicine, North Haven, CT, USA. [3]Singapore Immunology Network (SIgN), Singapore, Singapore. [4]Albert Einstein College of Medicine, New York, Seattle, WA, USA. [5]Department of Bioinformatics, The University of Texas Southwestern Medical Center, Dallas, TX, USA. [6]Department of Biomedical Engineering, University of Houston, Houston, TX, USA. [7]Department of Pediatrics, The University of Texas Southwestern Medical Center, Dallas, TX, USA. [8]Department of Pathology, The University of Texas Southwestern Medical Center, Dallas, TX, USA. [9]Department of Internal Medicine, The University of Texas Southwestern Medical Center, Dallas, TX, USA. [10]Feinberg School of Medicine, Northwestern University, Chicago, IL, USA. e-mail: shaheenmkhan@outlook.com

antibody-induced nephritis and lupus[18]. Previously, *Sle3a* interval has been shown to be associated with T cell hyperactivity, and *Sle3*-derived DCs and macrophages have been shown to be significantly more mature/activated and more proinflammatory[19–21]; however, no candidate genes have been identified associated with these phenotypes. The goal of this study was to identify the candidate gene within the lupus susceptibility locus *Sle3a*.

Numerous studies indicate that SLE has abnormalities in humoral immunity in conjunction with abnormal T-cell function[18,22,23]. Several groups have reported phenotypic and functional alterations in lupus T cells, including expansion of the Th17 population, perturbations in T-cell receptors (TCRs), and post-receptor downstream signaling that result in exaggeration of TCR response to stimuli and the propensity of lupus T cells to become more activated[24–27]. In addition, aberrant activation of DCs, defective clearance by macrophages and neutrophils, dysregulated macrophage polarization, and aberrant activation of several TLR pathways may lead to the initiation and perpetuation of SLE[28–30]. Thus, the observed hyperactivity in *Sle3* T cells can be due to T-cell intrinsic defects or due to abnormal regulation of T cells by DCs and macrophages[31–34]. Moreover, IFN-γ produced by Th1 cells plays a critical role in the production of antinuclear autoantibodies in murine lupus models[35]. Additionally, the secretion and function of several proinflammatory cytokines play a crucial role in the pathogenesis of SLE. Thus, a multitude of dysregulated immune cells and aberrant signaling pathways within the *Sle3a* interval may lead to SLE pathogenesis.

In this study, we present a complete fine-mapping analysis of the genomic interval containing the *Sle3a* locus by generating a series of truncated congenic recombinants that map the position of the *Sle3a* locus into a smaller genomic segment of approx. 2 Mb (*Sle3k*). Using whole-genome sequencing combined with RNA-seq, ATAC-seq, and functional assays, we identified *Klf13* as the primary candidate gene with increased expression in *Sle3k* compared to B6 mice. KLF13 is a member of the Krüppel-like family of transcription factors involved in the development of B and T cells at multiple stages[36–38] It positively regulates the expression of the chemokine RANTES 3-5 d after activation of T cells and is shown to be important for IL-4 signaling[39–42]. Although KLF13 has been shown to play an essential role in immune regulation and cancer, its role in lupus pathogenesis is unknown. Here, we identify *Klf13* as the lupus susceptibility gene and show that upregulation of *Klf13* in *Sle3k*-derived CD4 T cells was associated with changes in global gene expression and increased production of RANTES, IL2, and IFNγ following stimulation with anti-CD3 and anti-CD28. A subset of genes upregulated in *Sle3k* mice was markedly downregulated in *Klf13* $^{-/-}$ mice, including IL2 and IFNγ. Additionally, BMDMs derived from *Sle3* mice displayed increased expression of activation markers such as CD80, CD86, and MHCII, enhanced responsiveness to TLR signaling, and higher levels of proinflammatory cytokines and chemokines. We also observed increased infiltration of lymphocytes and production of RANTES, a key chemokine in lupus nephritis in the kidneys of *Sle1Sle3k* mice. In contrast, *Klf13* $^{-/-}$ mice exhibited a significant reduction of proinflammatory cytokines compared to wild-type mice and displayed striking dysregulation in several cytokines signaling pathways in both T cells and myeloid cells. ATAC-seq data revealed differences in the chromatin state in enhancer and promoter regions of key proinflammatory cytokines and chemokines such as IL-12β, TNFα, and CCL2 in macrophages and DCs derived from WT versus *Klf13* $^{-/-}$ mice and these results are coherent with genome-wide transcription changes observed by RNA-seq analysis. Thus, our findings reveal *Klf13* as a key lupus susceptibility gene that mediates a damaging proinflammatory state when combined with a breach in tolerance, in part, by modifying the chromatin landscape of inflammatory mediators resulting in hyperactive autoreactive T cells and dysregulated APCs to cause lupus pathogenesis.

Results

Fine mapping of *Sle3* interval using congenic dissection strategy

Sle3 interval has been previously shown to be associated with T cell hyperactivity and more activated and proinflammatory myeloid cells. We have previously established that the larger *Sle3* interval consists of two smaller congenic intervals, *Sle3a* (158–233) and *Sle3b* (157–158), that can independently act with *Sle1* to drive severe disease. Kallikreins were identified as a disease-associated gene cluster with the *Sle3b* locus. In this study, we performed fine mapping of *Sle3a* genomic interval by generating a series of truncated recombinants to identify candidate genes within the *Sle3a* as shown in Fig. 1a. We generated these recombinant strains by backcrossing of *Sle3* mice to B6 *mice* assisted with microsatellite markers. We then performed rigorous phenotyping of these recombinants for enhanced effector functions of modulation of different toll-like receptor signaling pathways in myeloid cells by stimulating Bone marrow-derived macrophages (BMDMs) and Bone marrow-derived dendritic cells (BMDCs) from 2–3 mo. old *Sle3* recombinant or B6 mice with TLR4 ligand (LPS) or TLR7 ligand (R8487). As previously reported, *Sle3t*- derived myeloid cells were more activated and hyperresponsive to toll receptor ligands. *Sle3t* -BMDMs displayed strikingly high expression of activation markers such as CD40 (Fig. 1b) and significantly increased production of proinflammatory cytokines TNFα and IL-6 (Fig. 1c,d). For the truncated recombinants, we observed significantly increased Mean fluorescence intensity (MFI) of cell surface activation markers, including CD80, CD40, CD86, and MHCII on BMDMs and BMDCs derived from the *Sle3* (157–233), *Sle3a* (158–233), *Sle3* (91–233) *and Sle3* (176–233) (Fig. 1e–h). Moreover, proinflammatory cytokines IL-6 and TNFα were produced at much higher levels in cultures of *Sle3* (91–233) *and Sle3* (176–233) congenic mice compared to B6 (Fig. 1i). In contrast, recombinants *Sle3* (158–211) *and Sle3* (231–233) did not show increased MFI of activation markers or enhanced production of proinflammatory cytokines (Fig. 1e–i), thus leading the mapping to the genomic interval 176–231. We then introgressed *Sle3a* and *Sle3b* onto *Sle1* to generate the bicongenic *Sle1.Sle3a* and *Sle1Sle3b* mice to perform phenotypic characterization by comparing these mice to B6, *Sle1*, full-length *Sle3t*, and *Sle1Sle3t mice*. As shown in Fig. 2a,b, *Sle1Sle3a and Sle1Sle3b* mice at four months and six months of age exhibited significantly higher levels of ANA. Consistent with our previous reports, the full-length *Sle1Sle3t* mice exhibited significantly higher levels of ANA, increased GN, and increased splenic weight leading to severe disease. As expected, *Slet, Sle3a*, and *Sle3b* intervals alone did not exhibit higher titers of ANA or any evidence of kidney disease. Additionally, *Sle1Sle3a* mice showed increased sensitivity to anti-GBM antibody-induced nephritis (AIGN) marked by elevated proteinuria and severe nephritis on Day 14 (Fig. 2c,d). Based on the phenotypic characterization of congenic mice, we localized the susceptibility loci into a smaller interval *Sle3k* (176–231) marked with D7Mit176 and D7Mit231 that contains one or more genes driving hyperactivation of myeloid cells and leading to lupus nephritis when combined with *Sle1*. This recombinant strain with the smallest congenic interval impacting the phenotypes was rescued, labeled *Sle3k, and* was then introgressed onto *Sle1* to produce the bicongenic *Sle1Sle3k* mice for further phenotypic characterization and candidate gene identification (Fig. 1a).

Sle3k mediates fatal lupus nephritis when combined with *Sle1*

Previous studies have demonstrated that the combination of *Sle1* and *Sle3* leads to severe GN with greater than 90% penetrance and mortality of ~60% by 12 months of age. Here, we investigated the effects of *Sle3k* in accelerating autoimmune phenotypes when combined with *Sle1* by producing 11-month-old aging cohorts of B6, *Sle1*, and *Sle1Sle3k* mice. *Sle1Sle3k* mice showed significantly increased splenic weight, proteinuria, and BUN levels (Fig. 3a–c). We performed pathological characterization of kidneys from these mice for glomerulonephritis (GN). *Sle1Sle3k* mice showed significantly higher GN score compared to *Sle1* (Fig. 3d,e). Next, we looked at the IgG ANA levels, a hallmark feature of lupus, and we show here that at 11- months of age, *Sle1Sle3k* mice produced much higher levels of IgG ANA compared to *Sle1* (Fig. 3f). In addition, we utilized an autoantigen array consisting of 96 autoantigens to check for IgG antibodies against a broad spectrum of autoantigens in these mice (Fig. 3g). Sera from 6–7 month-old *Sle1Sle3k* mice showed much higher reactivity to more than 70 autoantigens on the arrays, including glomerular and nuclear antigens. It has been shown that enhanced autoantibody production leads to immune infiltration in kidneys resulting in

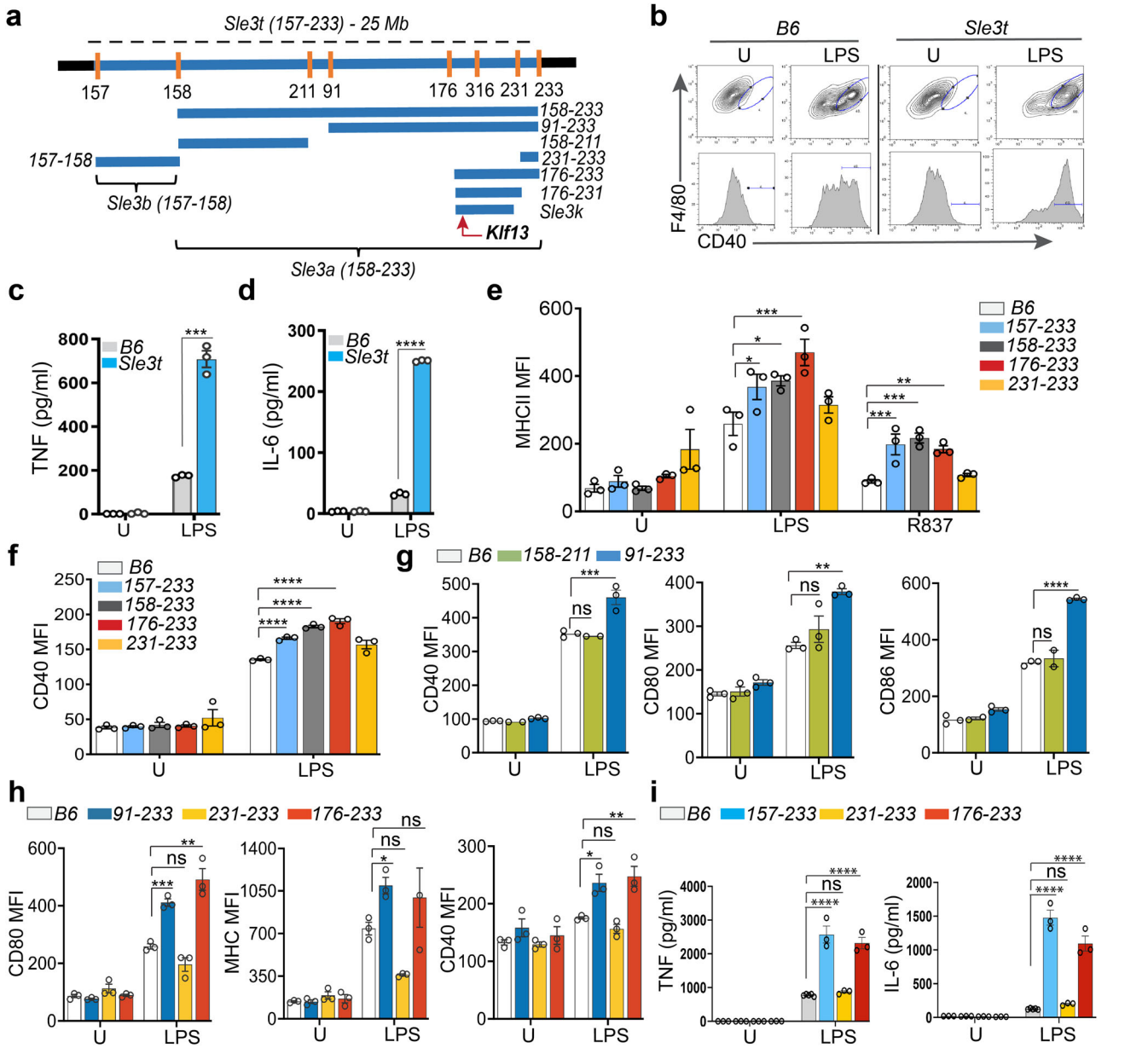

Fig. 1 | Congenic dissection of *Sle3* interval. a Diagrammatic representation of B6 congenic mouse interval harboring NZM2410- derived lupus susceptibility locus *Sle3t* flanked by D7mit157 and D7Mit233 on Chromosome 7 and all the *Sle3t*-derived truncated congenic intervals produced in the study for fine-mapping and gene identification. **b** Flow cytometry analysis showing CD40 expression BMDMs [unstimulated (U) or stimulated with LPS] derived from B6 or *Sle3t* strains. $N = 3$ mice per group. BMDMs cultured from B6 *and Sle3t* mice were unstimulated (U) and stimulated with 10 ng/ml LPS for 6 h, and supernatants were analyzed by ELISA for TNFα (**c**) and IL-6 (**d**). $N = 3$ mice per group. Values below the detection levels in ustimulated samples were assigned a value of 1. Mean fluorescence intensity (MFI) of CD40, MHCII, and CD80 on BMDMs [unstimulated (U) or stimulated with LPS] derived from B6 and different truncated *Sle3* recombinant strains is shown in **e**–**h**. $N = 3$ mice per group. **i** BMDMs cultured from B6 *and truncated Sle3* recombinant mice were unstimulated (U) and stimulated with 10 ng/ml LPS for 6 h, and supernatants were analyzed by ELISA for TNFα and IL-6. $N = 3$–5 mice per group. Each data point represents a single mouse in the figures. Student's *t*-test was performed for statistical analysis. Results are shown as means ± SEM. Statistical significance is represented as $^{*}p < 0.05$, $^{**}p < 0.01$, $^{***}p < 0.001$, $^{****}p < 0.0001$.

enhanced production of local cytokines and chemokines such as RANTES, leading to further inflammation. Therefore, we performed immunohistochemistry on kidney sections from aged mice and stained them with CD3 and RANTES antibodies. We saw significantly enhanced staining of CD3-positive cells and an increased number of tubules positively stained for RANTES in *SleSle3k* mice compared to *Sle1* mice (Fig. 3h–j). Importantly, *Slek* profoundly impacted T cell activation. We isolated CD4 T cells from the spleen of 2–3-month-old mice and stimulated them with plate-bound anti-CD3 and anti-CD28 for various time points. We found increased production of IL2 and IFNγ at 18 h and RANTES at 96 h post-stimulation in cultures of *Sle3k* CD4 T cells vs. B6 (Figs. 4d and 5a). Altogether, these results demonstrated that *Sle3k*, combined with *Sle1*, accelerates the autoimmune phenotypes and harbors one or more genes that drive the disease from benign to severe pathogenic autoimmunity.

Identification of *Klf13* as the lupus susceptibility gene within *the Sle3k* interval

Our first step toward identifying the candidate gene within *Sle3k* was to assess the gene expression changes within the identified critical region between D7Mit176 and D7Mit231. We performed RNA sequencing (RNA-seq) in CD4 T cells from *Sle3* mice with or without *Sle3k* region and *looked* at the expression of all the genes within the interval. There are more than 20

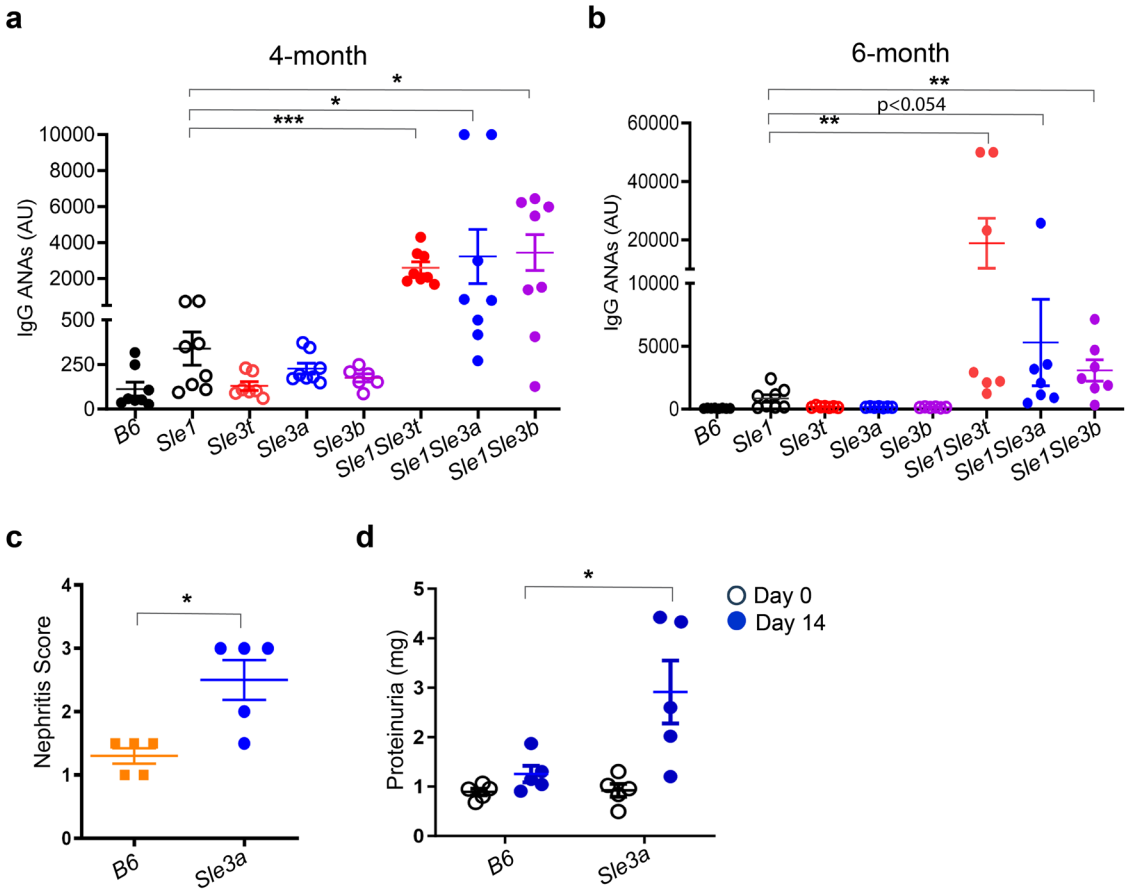

Fig. 2 | Phenotypic characterization of *Sle3* congenic mice. Assessment of serum levels of anti-nuclear autoantibodies (IgG) by Elisa in 4-month-old females (**a**) and 6–7-month old females (**b**). In panel **a**, B6 $n = 8$; *Sle1* $n = 8$; *Sle3t* $n = 7$; *Sle3a* $n = 8$; *Sle3b* $n = 6$; *Sle1Sle3t* $n = 8$; *Sle1.Sle3a* $n = 8$; *Sle1.Sle3b* $n = 8$. In panel B, B6 $n = 8$; *Sle1* $n = 8$; *Sle3t* $n = 7$; *Sle3a* $n = 7$; *Sle3b* $n = 6$; *Sle1Sle3t* $n = 7$; *Sle1.Sle3a* $n = 7$; *Sle1.Sle3b* $n = 7$. **c** Anti-GBM disease was induced in 6–12-week-old B6, and *Sle3a* strains and nephritis score was calculated at day 14 ($n = 5$ mice per group). **d** Twenty-four-hour urine samples collected from 2–3-month-old female mice on days 0 and 14 after the anti-GBM challenge were assessed for proteinuria ($n = 5$ mice per group). All mice used in this study are females. Each data point represents a single mouse in the figures. Results are shown as means ± SEM. Statistical significance is represented as $^{*}p < 0.05$, $^{**}p < 0.01$, $^{***}p < 0.001$, $^{****}p < 0.0001$.

genes within the *Sle3k* interval; however, only two genes, *Klf13* and *Mcee*, were differentially expressed at RPKM above 5 in unstimulated splenic CD4 T cells isolated from B6 and *Sle3k* based on RNA-seq analysis. The following reasons suggested the likelihood of *Klf13* as the candidate gene: First, based on RNA-seq data, the NZW allele of *Klf13* located within *Sle3k* interval is expressed at higher levels than the B6 allele (Fig. 4a). To confirm the upregulation of *Klf13* mRNA levels in *Sle3k* mice, Real-time PCR analysis was performed for the *Klf13* gene on RNA isolated from splenic CD4 T cells from B6 and *Sle3k* mice. Our analysis showed average 1.5-fold induction of *Klf13* mRNA levels in *Sle3k* compared to B6 (Fig. 4b). Second, the *Klf13 gene* was expressed at much higher levels in unstimulated CD4 T cells than *Mcee* and was expressed at very high levels in multiple immune cell lineages in the Immgen database and our laboratory RNA-seq database of human and mouse immune cells. Third and most importantly, KLF13 protein was induced at significantly higher levels in *Sle3k* compared to B6 at day 4 and day 5 post-stimulation (Fig. 4c). Previous studies have shown that *Klf13* is involved in T cell activation and the upregulation of chemokine RANTES in T cells. We, therefore, investigated the RANTES production and KLF13 protein expression in *Sle3k* CD4 T cells by stimulating them with anti-CD3 and anti-CD28 for multiple time points. We observed significantly increased RANTES production in *Slek*-derived CD4 T cells compared to B6 on day 4 (Fig. 4d). Next, we performed whole-genome sequencing on NZM2410, from which *Sle3* was initially derived to investigate genomic variations in the *Sle3k* region. In addition, we also did whole-genome sequencing of NZW and NZB, the two parental strains of NZM2410 (Fig. 4e). Each genome was aligned to the B6 reference genome, and variants were called using GATK. Our SNP analysis of genomes revealed that NZM2410-*derived Sle3k* is identical to a region in the NZW genome, as expected, as shown in Fig. 4e. High-quality variants covered by at least four sequence reads within the *Sle3k* interval were considered for further analysis. We analyzed genomic sequence data and found more than 1000 variants called within the *Sle3k* interval and six variants in the *Klf13* gene (Fig. 4f). In our sequencing data; we did not find any non-synonymous variant or a variant in the promoter region of *the Klf13* gene; however, there were five intronic variants, one 3-prime UTR variant and one variant, upstream of the transcription start site in the proximal enhancer region of *Klf13* gene. Considering the insights into the role of regulatory variants in gene regulation based on ENCODE data, these noncoding variations could potentially regulate the expression of the *Klf13* gene. To assess the impact of noncoding variation, we performed Assay for Transposase Accessible Chromatin with high-throughput sequencing (ATAC-seq), a method for mapping chromatin accessibility genome-wide, on splenic CD4 T cells and BMDMs isolated from B6 and *Sle3k* mice. Peaks indicative of open chromatin at the enhancer and the promoter regions of the *Klf13* gene in our CD4 and BMDMs datasets were in complete alignment with those observed in mouse Encode ATAC-seq datasets available in USCS genome browsers (Fig. 4g). Further analysis of our ATAC-seq data and publicly available CHIP-seq, ATAC-seq, and other regulatory datasets in the UCSC genome browser, Ensemble build, and CHIP Atlas revealed that the intronic variants at position 7:63,904,417, 7: 63,919,320 and 7: 63,921,779 and the upstream variant 7: 63939829 are nearby epigenetic marks and overlaps with peaks identified by ATAC-seq data and other regulatory sites (Fig. 4h). These

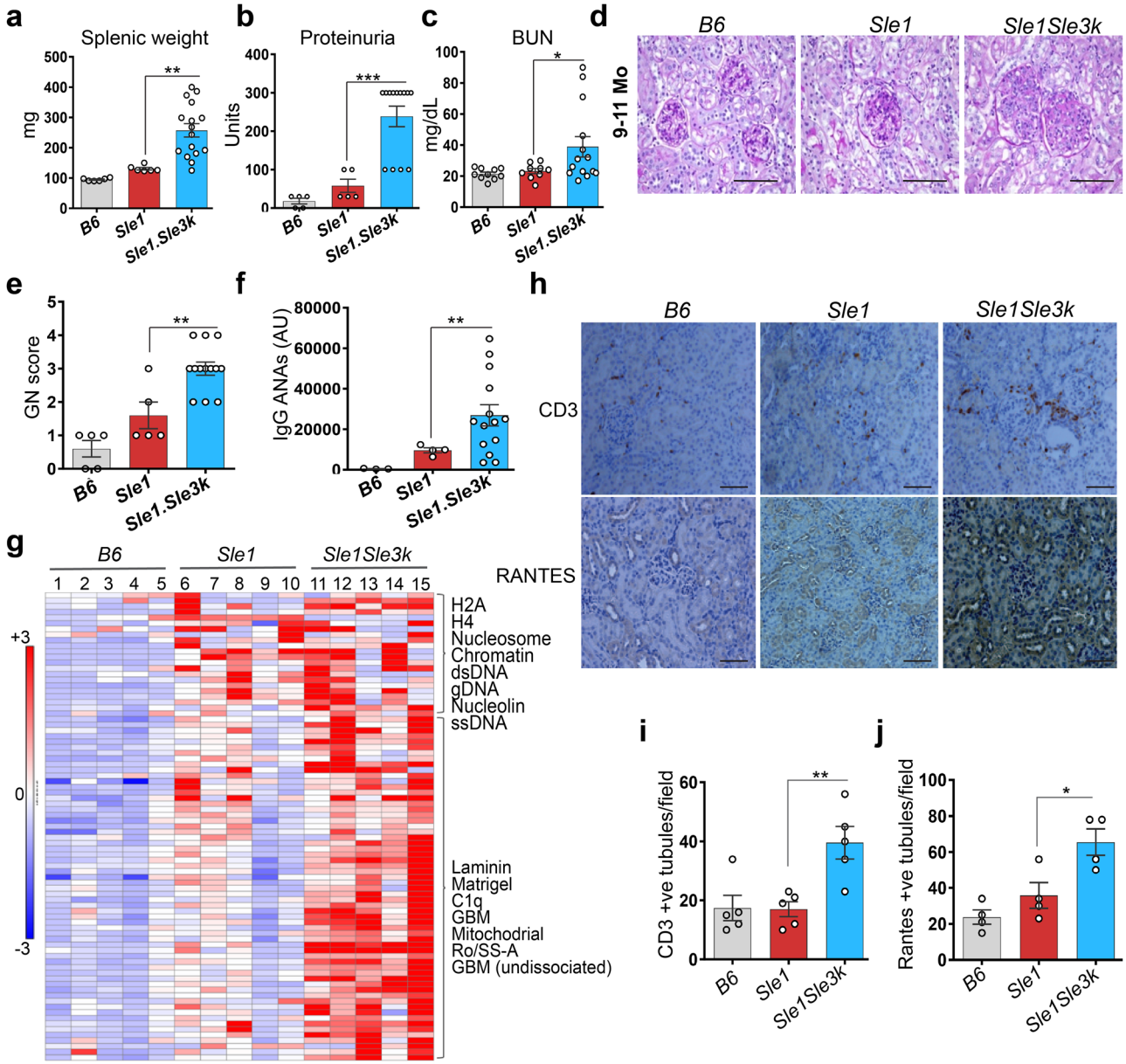

Fig. 3 | Phenotypic characterization of *Sle1Sle3k* congenic mice. a Measurement of splenic weight in *Sle1Sle3k* ($n = 16$) mice *versus* B6 ($n = 6$) and *Sle1* ($n = 6$) mice. **b** Measurement of proteinuria in *Sle1Sle3k* ($n = 13$) mice *versus* B6 ($n = 5$) and *Sle1* ($n = 5$). **c** Serum levels of BUN in *Sle1Sle3k* ($n = 14$) mice *versus* B6 ($n = 10$) and *Sle1* ($n = 9$). **d** Representative H & E slides showing the development of severe glomerulonephritis (GN) in kidneys of *Sle1.Sle3k* ($n = 13$) mice compared to B6 ($n = 5$) or *Sle1* ($n = 5$) mice at 9–12 months of age. Arrows indicate hyper-cellularity observed in glomeruli. Sacle bars, 100 µm. **e** GN scores graded in a blinded fashion are shown in *Sle1.Sle3k* mice ($n = 13$) compared to B6 ($n = 5$) or *Sle1* ($n = 5$) mice at 9–12 months of age. **f** Serum levels of anti-nuclear autoantibodies (IgG) in *Sle1.Sle3k* mice ($n = 14$) compared to B6 ($n = 3$) or *Sle1* ($n = 4$) were assessed by Elisa. **g** Heatmap depicting increased serum autoantibody titers in *Sle1Sle3k* mice compared to B6 and *Sle1* mice against a panel of 96 autoantigens spotted on a custom array. Mice per group ($n = 5$). **h** Representative images of immunohistochemistry for CCL5 and CD3 of paraffin-fixed kidney sections of 9–12-month-old mice. Quantification of tubules stained for CD3 +ve cells per field (**i**) and RANTES +ve tubules per field (**j**) in kidney sections is shown. $N = 4$-5 per strain. Scale bars, 100 µm. All mice used were 9–12-month-old females for all three strains. Each data point represents a single mouse in the figures. Results are shown as means ± SEM. Statistical significance is represented as $^{*}p < 0.05$, $^{**}p < 0.01$, $^{***}p < 0.001$, $^{****}p < 0.0001$.

results suggest a potential role of these regulatory variants in modifying the chromatin accessibility of the *Klf13* enhancer region, thereby resulting in increased levels of *Klf13* mRNA in *Slek* mice. Taken together, our phenotypic and genomic data revealed *Klf13* as the lupus susceptibility gene within *Sle3k*.

Klf13 impacts global gene expression and activation of CD4 T cells in *Sle3k* mice

Our initial characterization had shown that full-length *Sle3* interval also affects CD4 T cell phenotype. This led us to investigate whether *Sle3k* harboring *Klf13* impacts CD4 T cell activation. To address this question, we isolated CD4 T cells from the spleen of 2–3-month-old mice, stimulated them with plate-bound anti-CD3 and anti-CD28 for various time points, and measured the production of different cytokines. We found increased production of IL2 and IFNγ at 48 h post-stimulation in cultures of *Sle3k* CD4 T cells vs. B6 (Fig. 5a). Since KLF13 is known to regulate RANTES in T cells, we measured RANTES production in CD4 T cell cultures 96 hours after stimulation with anti-CD3 and anti-CD28 (0.5 ug/ml or 1 ug/ml). We found a striking increase in the production of RANTES in cultures of *Sle3k* CD4 T cells compared to B6 (Fig. 4d). This increased RANTES levels in

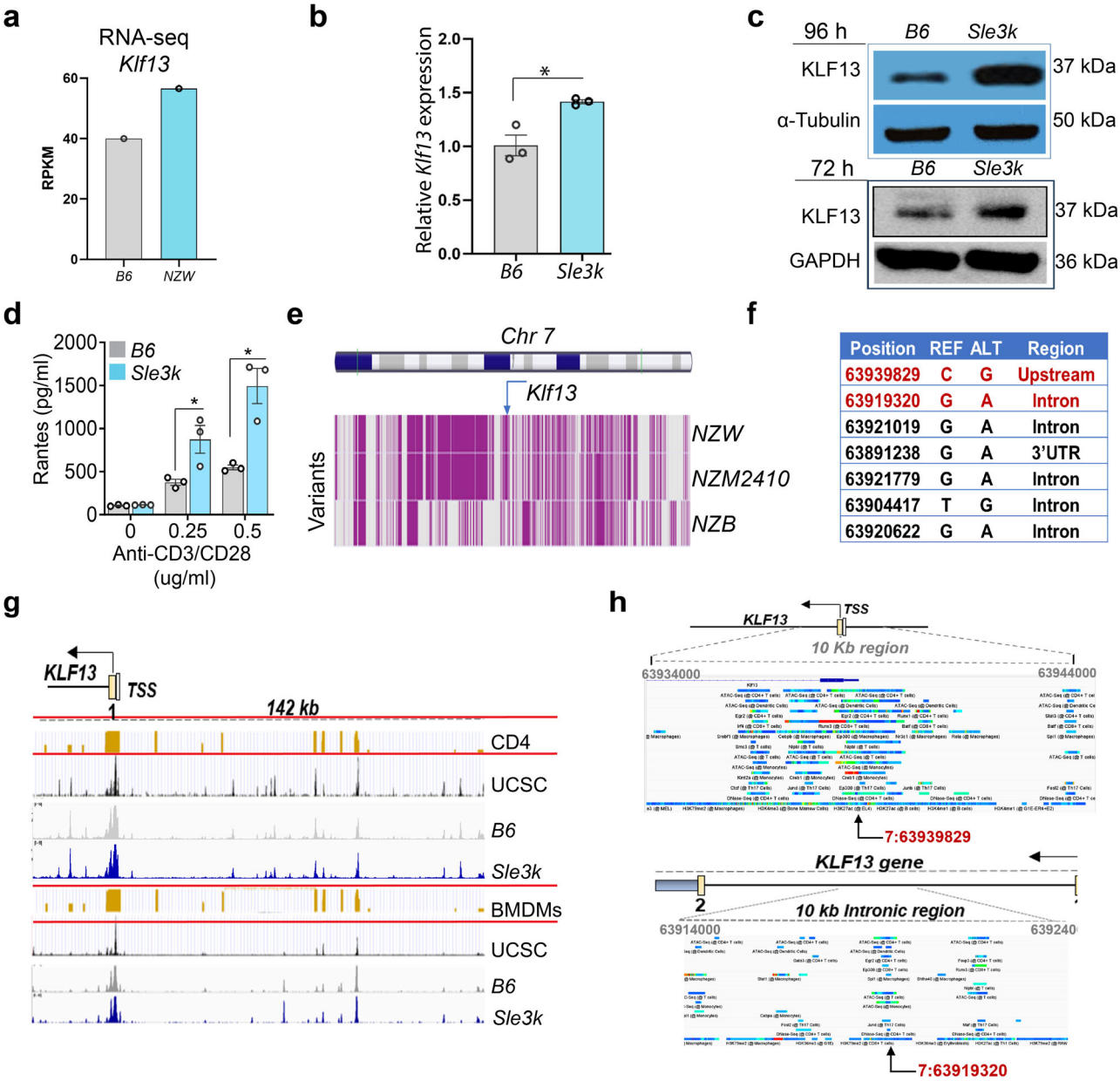

Fig. 4 | Identification of *Klf13* as a lupus susceptibility gene. a RPKM gene expression values of NZW allele versus B6 allele of *Klf13* gene in splenic CD4 T cells assessed by RNA-seq ($n = 1$). **b** Real-time PCR analysis of KLF13 mRNA levels measured in splenic CD4 T cells isolated from B6 *versus Sle3k* ($n = 3$ mice per group). **c** Western blot showing KLF13 protein expression in splenic CD4 T cells isolated from B6 *versus Sle3k* mice at 72 h and 96 h post-stimulation with anti-CD3/anti-CD28. GAPDH and KLF13 protein run at the same size and hence the bands shown for 72 h post timepoint are from two separate gels. **d** Splenic CD4 T cells were stimulated with plate-bound anti-CD3/anti-CD28 for 96 h, and levels of RANTES was measured by ELISA ($n = 3$ per group). **e** Whole genome sequencing of NZB, NZW, and NZM2410 mouse strains depicting the mapping of *Sle3k* congenic interval on Chr7. All the variants in three mouse strains compared to the B6 genome are colored in purple. **f** All SNPs in the NZW allele of the *Klf13* gene were identified by genome sequencing. **g** Comparison of ATAC-seq data from CD4 T cells and BMDMs in B6 (Gray Panel) *versus Sle3k* (Blue Panel) mice. Bedgraph panels for the *Klf13* gene are shown with peak locations relative to the transcription start site (TSS). The top Black panels are the ATAC-seq Bed files of mouse Encode data obtained from the UCSC genome browser. Yellow bars indicate regulatory elements identified in Ensemble regulatory build. **h** Bedgraph panels generated from CHIP Atlas data for the *Klf13* gene shown for multiple immune cells including CD4 T cells and the position of upstream variant 7:63939829 within the epigenetic mark overlapping with the peak of regulatory regions and several transcription factors binding sites as indicated by black arrow in the Top panel. The position of the intronic variant 7: 63919320 is shown nearby to the peak regulatory signal in the intron is shown in bottom panel indicated by black arrow. Results are shown as means ± SEM. Statistical significance is represented as $^{*}p < 0.05$, $^{**}p < 0.01$, $^{***}p < 0.001$, $^{****}p < 0.0001$.

Sle3k mice was associated with increased KLF13 protein expression in *Sle3k* mice compared to B6 at 72 h and 96 h post-stimulation, directly supporting the role of KLF13 in CD4 T cell activation in lupus mice (Fig. 4c). These results were coherent with observed increased levels of chemokine RANTES in the kidneys of *Sle31Sle3k* mice, as shown in Fig. 3j. To further decipher the role of KLF13 in T cell activation in *Sle3k* mice, we performed RNA-seq analysis on CD4 T cells from B6 and *Sle3k* stimulated with anti-CD3 and anti-CD28 for 6 h and 18 h. RNA-seq data revealed global gene expression changes in *Sle3k* CD4 T cells compared to B6, with more than 100 genes differentially regulated between the two strains (Fig. 5b). Importantly, gene expression levels of IL2 and IFNγ were significantly higher in *Slek* mice compared to B6 thereby supporting the Elisa data (Fig. 5b). These results indicated KLF13 as a key transcriptional factor within the *Sle3k* interval in enhancing T-cell activation. To demonstrate the role of the *Klf13* gene in the

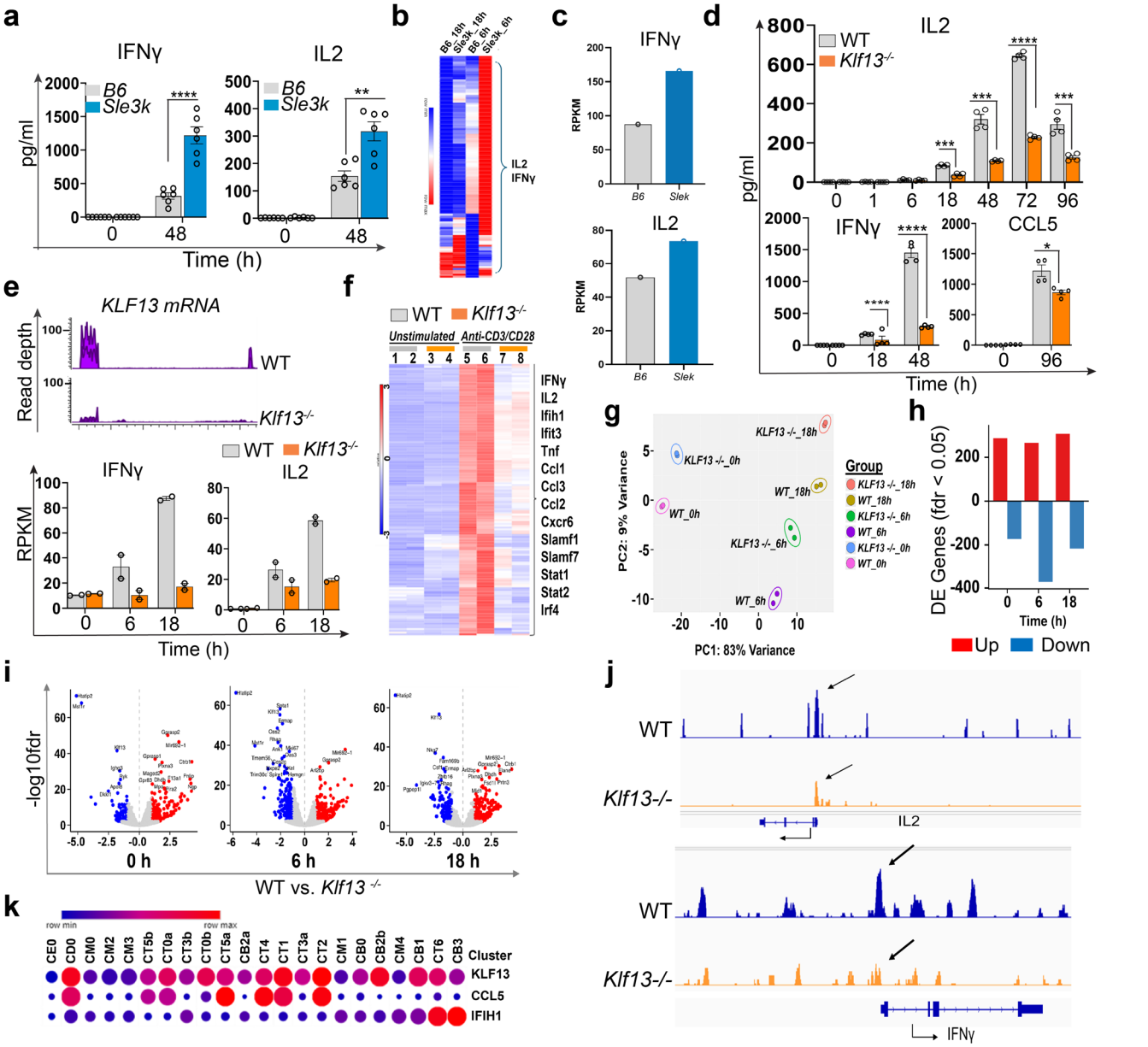

Fig. 5 | Regulation of T cell activation and production of proinflammatory cytokines mediated by KLF13. a Splenic CD4 T cells were stimulated with plate-bound anti-CD3/anti-CD28 for 48 h and levels of IL2 and IFNγ in the cell culture supernatants were determined by ELISA ($n = 6$ per group). **b** Heatmap of differentially regulated selected genes in splenic CD4 T cells isolated from B6 *versus Sle3k* mice as determined by RNA-seq analysis at 6 h post-stimulation with anti-CD3/anti-CD28. **c** Gene expression values for IL-2 and IFNγ are shown as determined by RNA-seq analysis of CD4 T cells isolated from B6 *versus Sle3k* mice. **d** Splenic CD4 T cells were stimulated with plate-bound anti-CD3/anti-CD28 for different time points (hour), and levels of IL2, IFNγ, and CCL5 in the cell culture supernatants were determined by ELISA in *Klf13*$^{-/-}$ versus *WT* mice ($n = 4$). **e** RNA-seq panels showing the read depth of KLF13 mRNA level confirming the knockdown of *the Klf13* gene in *Klf13*$^{-/-}$ mice compared to *WT* mice. RPKM gene expression values for IFNγ and IL-2 are shown as determined by RNA-seq analysis of CD4 T cells isolated from *Klf13*$^{-/-}$ versus *WT* mice. **f** Heatmap of differentially regulated genes in splenic CD4 T cells isolated from *Klf13*$^{-/-}$ mice *versus WT* mice as determined by RNA-seq analysis at 18 h post-stimulation with anti-CD3/anti-CD28. $N = 2$ experiments. **g** PCA analysis of RNA seq data of unstimulated or CD4 T cells stimulated with anti-CD3/anti-CD28 for 6 h and 18 h isolated from *Klf13*$^{-/-}$ versus *WT* mice. **h** Bar graph showing number of significantly variable genes between *Klf13*$^{-/-}$ versus *WT* mice with FDR < 0.05 and LOG10 fold change greater than one. **i** Volcano plot comparing RNA seq data in *Klf13*$^{-/-}$ versus *WT* mice in unstimulated and stimulated CD4 T cells at 6 h and 18 h post-stimulation (anit-CD3 and anti-CD28) by plotting the fold change on the x-axis and -log10 of the *p*-value on the y-axis. **j** ATAC-seq was performed on CD4 T cells unstimulated or stimulated with anti-CD3/anti-CD28 for 3 h isolated from *Klf13*$^{-/-}$ versus *WT* mice. $N = 2$. Bedgraph panels for IL2 (0 h) and IFNγ (3 h) are shown with peak locations relative to the transcription start site (TSS). **k** *Klf13*, *Ccl5*, and *Ifih1* gene expression in the various cell subsets in published single cell datasets of kidney biopsies from Lupus Nephritis (LN) patients[43]. Cell cluster annotations are as follows: CE0- Epithelial cells ; CD0- dividing cell cluster including T cells and NK cells; CM0, CM1 and CM4 are monocyte/macrophage clusters; CM2- Macrophages; CM3- CD1C+ dendritic cells (DCs); CT1 and CT5b are NK cell clusters; CT0a, CT3b, CT0b, CT2, CT3a and CT5a, and CT4 are T cell clusters; CB2a and CB0 are B cell clusters; CB2b- plasmacytoid DCs (pDCs); CB1- plasma cells/plasmablasts; CT6- CD4 + T cells with high levels of ISGs; CB3- B cells with high levels of ISGs. Results are shown as means ± SEM. Statistical significance is represented as $^{*}p < 0.05$, $^{**}p < 0.01$, $^{***}p < 0.001$, $^{****}p < 0.0001$.

production of key inflammatory cytokines and global gene expression changes leading to enhanced CD4 T cell activation, we utilized *Klf13* $^{-/-}$ mice generated in Dr. Carol Clayberger's laboratory at Northwestern University. We used similar experimental conditions and isolated splenic CD4 T cells from 2–3-month-old *Klf13*$^{-/-}$ mice or wild-type mice and stimulated with plate-bound anti-CD3 and anti-CD28 for various time points and measured the production of different cytokines. We observed strikingly diminished production of IL2 at 18 h, 48 h, 72 h, and 96 h and IFNγ at 18 h and 48 h in cultures in *Klf13*$^{-/-}$ mice compared to wild-type mice (Fig. 5d). We also observed diminished levels of RANTES at 96 h in *Klf13*$^{-/-}$ as published by other groups (Fig. 5d). To further investigate the role of KLF13, we performed RNA-seq on CD4 T cells isolated from wild type, and *Klf13*$^{-/-}$ mice stimulated with anti-CD3 and anti-CD28 for 6 h and 18 h. Absence of *Klf13* mRNA levels in *Klf13*$^{-/-}$ CD4 T cells is confirmed in Fig. 5e, as shown by low read counts in *Klf13*$^{-/-}$ mice compared to the wild type. RNA-seq analysis revealed a dramatic reduction in IL2 and IFNγ mRNA levels in *Klf13*$^{-/-}$ mice both at 6 h and 18 h in accordance with Elisa data (Fig. 5e). Additionally, there was striking genome-wide repression of more than 300 genes involved in T cell activation in *Klf13*$^{-/-}$ mice, as observed in the heatmap and in the bargraph (Fig. 5f,h). Combined PCA analysis based on RNA seq gene expression data separated *Klf13*$^{-/-}$ mice and wild-type mice in distinct groups in unstimulated and post-stimulation conditions (6 h and 18 h) (Fig. 5g). More than 400 genes were significantly dysregulated (FDR < 0.05) in *Klf13*$^{-/-}$ mice compared to WT, as determined by the Deseq2 at 6 h and 18 h post stimulation and depicted in the bar graph and volcano plot (Fig. 5h,i). Comparative gene expression analysis of RNA-seq data from B6, *Sle3k*, WT, and *Klf13*$^{-/-}$ mice identified a subset of key genes (*IL2, IFNγ*, and more) that were significantly upregulated in *Sle3k* mice associated with the increased levels of *Klf13* in *Sle3k* compared to B6. These genes were significantly downregulated in *Klf13*$^{-/-}$ mice compared to wild-type mice. Ingenuity Pathway Analysis showed Th1 and Th2 as the top two canonical pathways inhibited in the absence of KLF13 in CD4 T cells both at 6 h and 18 h post-stimulation. We then performed ATAC seq on splenic CD4 T cells isolated from WT and *Klf13*$^{-/-}$ mice and stimulated with anti-CD3/anti-CD28 for 3 h. We observed reduced chromatin accessibility at the promoter and enhancer region of the IL2 and IFNγ genes in *Klf13*$^{-/-}$ mice compared to WT (Fig. 5j). To understand the role of KLF13 in lupus nephritis in patients, we analyzed the published single-cell datasets of kidney biopsies from lupus nephritis (LN) patients. *Klf13* was highly expressed in multiple immune cell subsets, including B cells (CB1, CB2b), T cells, and NK cells in LN kidneys[43]. Notably, *Klf13* gene expression levels were highly correlated with high levels of CCL5 gene expression in T cells in LN kidneys, supporting our current findings in mice. In addition, *the Klf13* gene was highly expressed in the CD4 positive T cell subset that demonstrated strikingly higher levels of interferon-stimulated genes (ISGs, including ISG15, MX1, RSAD2, OAS3, IFIT1, and IFIT2) (Fig. 5k).

KLF13 regulates toll receptor signaling in myeloid cells by altering the chromatin architecture of proinflammatory cytokines

BMDMs and BMDCs derived from full-length *Sle3* displayed enhanced responsiveness to TLR4 (LPS) and TLR7 (R837) (Fig. 1), and we used this phenotype to narrow down the *Sle3* interval to *Sle3k*. To further investigate whether *Sle3k* exhibits enhanced responsiveness to TLR ligands, BMDMs derived from B6 or *Sle3k* were either stimulated with LPS (TLR4) or R838 (TLR7/8) for 6 and 18 h and cytokines were measured in these cultures. We observed increased levels of several proinflammatory cytokines, such as TNF-α and CCL2 in response to LPS or R848 in BMDM cultures of *Sle3k* mice compared to B6 (Fig. 6a). RNA-seq analysis of BMDCs revealed more than 100 genes differentially expressed in response to R848 at 6 h post-stimulation in *Sle3k* vs. B6, as depicted in the heat map in Fig. 6b. Several proinflammatory cytokines/ chemokines such as *CCL3*, *TNFα*, *CCL12, CXCL10, CCL8* and *IL12a* mRNA levels were induced at much higher levels in *Sle3k*-derived BMDCs in response to toll receptor ligands. These results, taken together, suggested that *Sle3k*-derived myeloid cells not only produced elevated levels of cytokines but also exhibited a global proinflammatory gene expression profile. We hypothesize this heightened activation state of *Sle3k* is due to the upregulation of the *Klf13* gene in the *Sle3k* interval. To address this, we produced BMDMs from wild-type or *Klf13*$^{-/-}$ mice and stimulated them with different TLR ligands: LPS (TLR4), R848 (TLR7/8) and ODN1826 (TLR9) for 6 h. BMDMs from *Klf13*$^{-/-}$ mice produced diminished levels of CCL2 and TNFα (Fig. 6c) and showed a marked reduction in induced mRNA levels of *TNFα and CCL2* cytokine genes (Fig. 6d). We performed RNA seq analysis in unstimulated and stimulated BMDM cultures to assess the global transcription changes. As shown in Heatmap in Fig. 6d, genome-wide expression changes with more than 400 differentially regulated genes were observed in BMDMs derived from *Klf13*$^{-/-}$ mice versus wild type in response to TLR ligands. This strongly implicates a potential role of KLF13 in toll receptor signaling in BMDMs. Dendritic cells and TLR signaling play a key role in lupus pathogenesis. The role of *KLF13* in dendritic cell biology has been unknown. To investigate the role of *KLF13* in TLR signaling in dendritic cells, we cultured Bone-marrow-derived dendritic cells (BMDCs) in the presence of GMSCF and IL-4 and stimulated them with LPS (TLR4) and R838 (TLR7/8) for 6 h. We performed RNA seq analysis in unstimulated and stimulated BMDC cultures to assess the global transcription changes. As shown in the heatmap and bar graph, striking genome-wide expression changes with more than 500 differentially regulated genes (FDR < 0.05) were observed in BMDCs derived from *Klf13*$^{-/-}$ mice versus wild-type in response to TLR ligands at 6 h post-stimulation (Fig. 6e,f). *Klf13* knockout BMDCs exhibited attenuated mRNA levels of *IL-12β*, *CCL2*, and *IL-1β* in response to LPS and TLR7/8 as measured by RNA-seq. Combined PCA analysis based on RNA seq gene expression data separated *Klf13*$^{-/-}$ mice and wild-type mice in distinct groups in unstimulated and post-stimulation conditions (Fig. 6g). Comparative gene expression analysis and IPA analysis revealed genome-wide changes in expression profiles of several different chemokines and cytokines in *Klf13*$^{-/-}$ BMDCs, confirming the role of KLF13 as a key transcription in TLR signaling and regulation of inflammatory gene expression in dendritic cells. The pathway analysis revealed cytokine signaling as the significant dysregulated pathway in BMDCs without KLF13. Next, we investigated if the global gene expression changes observed in BMDMs and BMDCs are due to modification in the chromatin landscape mediated by KLF13. To address this, we performed ATAC-seq on BMDMs and BMDCs derived from *WT* and *Klf13*$^{-/-}$ mice stimulated with R848 for 1 h or 3 h timepoint. We observed reduced chromatin accessibility at the promoter and enhancer region of key proinflammatory genes, including *CCL2, IL12β*, and *TNfα* genes, as shown in Fig. 6h. Similarly, we observed reduced ATAC-seq peaks at *CCl2, IL6, IL12β*, TNfα and *CCL5* genes in *Klf13*$^{-/-}$ BMDCs compared to wild type Fig. 6i. The results of ATAC-seq data is in line with the downregulation of mRNA levels observed by RNA seq data in BMDMs and BMDCs derived from *Klf13*$^{-/-}$ mice compared to wild-type. These results demonstrate a key role of KLF13 in the upregulation of proinflammatory cytokines and chemokine and subsequently leading to hyperactivation of myeloid cells in response to toll receptor ligands.

Discussion

Gene identification of lupus susceptibility loci has been challenging due to the weak contributions of multiple loci toward the disease. We previously demonstrated that the large lupus susceptibility *Sle3t* (157–233) locus on chromosome 7 consisted of two independent loci, *Sle3a* (158–233), and *Sle3b* (157–158), that drive the pathogenic phenotype and that there is a strong epistatic interaction between *Sle1* and *Sle3* loci. While the Kallikreins were identified as a disease-associated gene cluster with the *Sle3b* locus, no candidate gene associated with the *Sle3a* locus has been identified. In this study, we presented the complete fine-mapping of the *Sle3a* interval and narrow it to a approx. 2 Mb region. Based on extensive genomic, phenotypic, and functional characterization, our study revealed *Klf13* as the key gene within the *Sle3a* interval responsible for driving inflammation and promoting lupus pathogenesis. We showed that *Sle3k* mice expressed higher levels of the *Klf13* gene and protein compared to B6. This upregulation of *Klf13* in *Sle3k* mice resulted in genome-wide transcription changes and

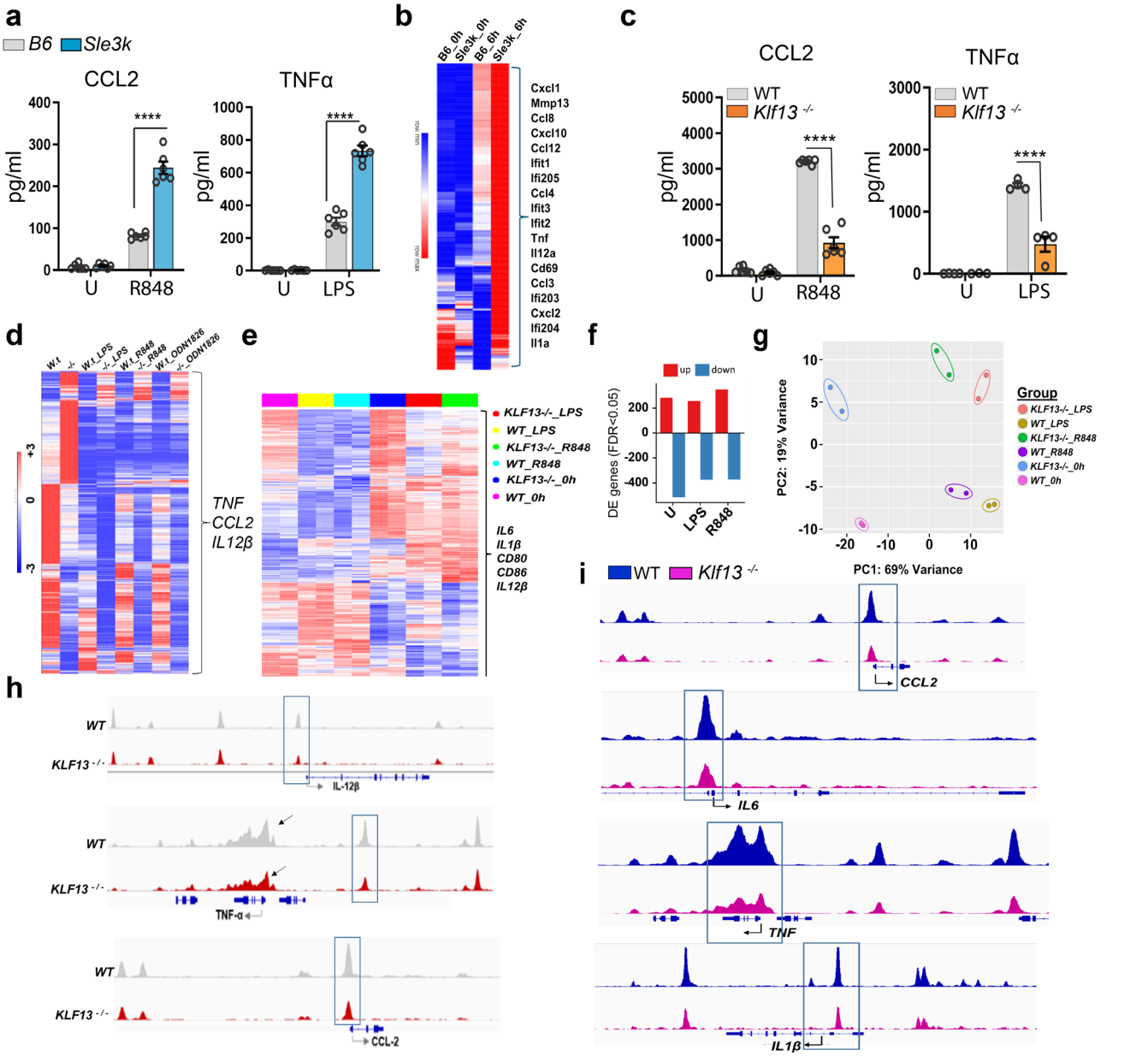

Fig. 6 | KLF13 modulates toll receptor signaling in myeloid cells. a BMDMs cultured from B6 *and Sle3k* mice were unstimulated and either stimulated with 1 mg/ml R848 or 10 ng/ml LPS for 6 h, and supernatants were analyzed by ELISA for CCL2 and TNFα, respectively ($n = 6$). **b** Heatmap of differentially regulated genes in BMDCs derived from *Sle3k* versus B6 mice unstimulated or stimulated with 1 mg/ml R848 for 6 h as analyzed by RNA-seq analysis. $N = 1$ per timepoint. **c** BMDMs cultured from WT versus *Klf13*$^{-/-}$ mice were unstimulated or stimulated with 1 mg/ml R848 or with 10 ng/ml LPS for 6 h, and supernatants were analyzed by ELISA for CCL2 ($n = 6$) and TNFα ($n = 4$) respectively. **d** Global gene expression profiling of BMDMs derived from wild type, and *Klf13*$^{-/-}$ mice either unstimulated or stimulated with 1 mg/ml R848 or 10 ng/ml LPS or 10 mg/ml ODN1826 for 6 h. $N = 1$ per timepoint. Heatmap represents differentially expressed genes between WT. and *Klf13*$^{-/-}$ mice determined by RNA-seq analysis. **e** Global gene expression profiling of BMDCs derived from wild type and *Klf13*$^{-/-}$ mice either unstimulated or stimulated with 1 mg/ml R848 or with 10 ng/ml LPS for 6 h. Heat maps represent differentially expressed genes between WT. and *Klf13*$^{-/-}$ mice determined by RNA-seq analysis at 6 h in response to LPS. $N = 2$ per time-point. **f** Total number of genes significantly upregulated or downregulated between wild type and *Klf13*$^{-/-}$ mice in each treatment group (FDR < 0.05). **g** PCA analysis of RNA seq data of BMDCs unstimulated or stimulated with LPS or R848 for 6 h isolated from *Klf13*$^{-/-}$ versus *WT* mice. ATAC-seq was performed on WT versus *Klf13*$^{-/-}$ derived BMDMs (**h**) and BMDCs (**i**) treated with 1 mg/ml R848 for 1 h or 3 h ($N = 2$ per time point). Bedgraph panels for CCL2, IL-12β, IL-1β, IL-6 and TNF-α are shown with peak locations relative to the transcription start site (TSS) highlighted by boxes and arrows. BMDMs, Bone-marrow derived macrophages; BMDCs, Bone-marrow derived dendritic cells. Results are shown as means ± SEM. Statistical significance is represented as $^{*}p < 0.05$, $^{**}p < 0.01$, $^{***}p < 0.001$, $^{****}p < 0.0001$.

increased production of several proinflammatory cytokines, partly via modifying their chromatin landscape, leading to the hyperactivation of T cells and myeloid cells. Thus, we propose that the proinflammatory phenotype mediated by KLF13 in *Sle3k* when combined with a breach in tolerance mediated by the *Sle1* locus, results in a damaging inflammatory state potentially via producing hyperactive self-reactive T cells and APCs that infiltrate the kidneys, thereby causing tissue damage as evidenced by increase tissue-specific autoantibodies, increased ANA, RANTES, and several other proinflammatory cytokines to ultimately cause fatal lupus nephritis. It is well established that hyperactive self-reactive T cells infiltrate tissues resulting in the destruction of target organs in autoimmune diseases. Previous studies implicated that the *Sle3* interval is associated with aberrant T-cell hyperactivity. Here, we presented extensive genomic and functional characterization of CD4 T cells in B6 and lupous-prone *Sle3k* mice. Our

results demonstrated that *Klf13* mRNA levels were significantly higher in *Sle3k* mice compared to B6 in CD4 T cells. There was a significantly higher induction of KLF13 protein in *Sle3k* CD4 T cells compared to B6 at day 3 and Day 4 post-stimulation. We showed profound genome-wide transcription and chromatin changes in CD4 T cells derived from *Sle3k* mice harboring the *Klf13* gene compared to B6. We measured *Klf13* mRNA and protein levels in several human and mouse immune cell types and observed that *Klf13* was most highly expressed by T cells, as shown in previous reports. One of the most striking effects of activated *Sle3k* CD4 T cells was significantly upregulated KLF13 protein levels in *Sle3k* mice, resulting in much higher upregulation of RANTES than B6 mice. In addition, increased RANTES expression was observed in the kidneys of aged *Sle1Sle3k* mice. Thus, the upregulated KLF13 levels leading to increased RANTES production and, consequently, recruitment of inflammatory cells in the Kidney may partly explain the underlying mechanism of observed lupus nephritis in *Sle1Sle3k* mice. In addition to RANTES, activated *Sle3k* CD4 T cells displayed increased gene expression levels, modified chromatin architecture, and increased production of IL-2, IFNγ, and several other proinflammatory cytokines. The role of KLF13 in *Sle3k mice* is supported by dramatic suppression of cytokine production and a striking reduction in RANTES levels at four days post-stimulation observed in *Klf13*$^{-/-}$ mice. It is worth noting that while most of the phenotypes described associated with the *Sle3* interval were reversed in *Klf13*$^{-/-}$ mice, some differences were noted. For example, the dampening of cytokines such as IL2 and IFNγ in CD4 T cells derived from *Klf13*$^{-/-}$ mice was much more profound than the upregulation observed in *Sle3k* mice. Several genes were uniquely modified in *Klf13*$^{-/-}$ mice that were not changed in *Sle3k* mice, suggesting that complete knockout of KLF13 has more profound changes than the upregulation of KLF13 in *Sle3k* mice. Nevertheless, taken together, our data strongly suggest that increased levels of KLF13 modify the expression of key proinflammatory cytokines resulting in potentially hyperactive self-reactive T cells that infiltrate the kidneys and cause tissue damage in part by producing increased levels of RANTES, proinflammatory cytokines, and increased tissue-specific autoantibodies in *Sle1Sle3k* mice. How these hyperactive CD4 T cells affect different immune cell types in the kidneys and periphery in lupus-prone mice remains to be studied.

A myriad of findings implicates the role of aberrant/hyperactive APCs in driving inflammation and autoimmunity. Previous studies showed that the large *Sle3* interval is associated with the hyperactivation of myeloid cells. In this study, we presented the in-depth functional characterization of BMDMS and BMDCs from *Sle3k* mice. We demonstrate that the *Klf13* is the gene responsible for the hyperactivation of *Sle3*-derived myeloid cells that display increased cell surface expression of costimulatory molecules CD80, CD40, and I-Ab, strikingly increased secretion of proinflammatory cytokines and dysregulated cytokine gene expression pathways. This profile was reversed in *Klf13* knockout mice that displayed profound genome-wide transcriptional changes in both cell types with a striking reduction in the production of key proinflammatory cytokines IL6, TNFα, and IL1β in response to toll receptor ligands. Based on pathway analysis in *Sle3k* and *Klf13*$^{-/-}$ mice, we conclude that KLF13 affects inflammation and autoimmunity by affecting major cytokine pathways and modulating toll receptor signaling in BMDMs and BMDCs. Furthermore, comparing the phenotypes conferred by *Sle3k* mice and *Klf13*$^{-/-}$ mice, our study pinpoints *Klf13* within the *Sle3k* interval as the gene responsible for the aberrant phenotypes of APCs and their hyperresponsiveness to toll receptor signaling. One study previously showed that miR-1251-5p, which targets KLF13, plays a crucial role in suppressing the classical activation of macrophages while promoting alternative activation[44]. Our study show that KLF13 is directly involved in modulating the function of innate immune cells leading to lupus pathogenesis. These aberrant APCs may partially be responsible for potentially generating hyperactive autoreactive CD4 T cells that infiltrate kidneys resulting in lupus nephritis.

Although the *Sle3k* interval harboring the *Klf13* gene is considerably large, based on our extensive genomic and functional studies, it is unlikely that there is another candidate gene that is driving the phenotype. However, it is possible that there could be lncRNA or microRNA within this relatively large interval contributing to the observed phenotypes in *Sle3k* mice. In Follow-up studies, a direct knockdown of *Klf13* in *Sle1.Sle3k* mice, in a cell type-specific manner, may reveal a deeper understanding of the role of KLF13 in SLE pathogenesis. Multiple lines of evidence in our study suggest *Klf13* as the primary candidate gene in lupus pathogenesis in *Sle3k* mice; however, it is likely that the variations in the noncoding regions of the *Sle3k* interval may also impact the observed phenotype. Future studies should focus on developing strategies to prioritize and functionally test the noncoding variations within the *Sle3k* interval in different cell types and states. Extensive effort is now being made in the field to assess the impact of noncoding variations, such as the Noncoding Variants Program (NoVa), to support the development of strategies and computational programs to prioritize and identify the variants in a region associated with disease and to assess the accuracy of predictions functionally. Recently, Mouri et al. developed an effective approach utilizing high-throughput allele-specific reporter assays to prioritize disease-associated variants for five autoimmune diseases[45]. Technological advancements, including high-resolution epigenomic studies, integrative data analysis, and the development of databases such as EpiMAp, will significantly help dissect the role of noncoding variations in driving disease pathology. Our long path to identify candidate genes within the lupus susceptibility interval in this study highlights the importance of complex genetics that underlie the pathogenesis of SLE. It also underscores the importance of understanding the functional consequences of noncoding variations and epigenetic regulation in promoting autoimmunity and inflammation. To our knowledge, KLF13 has not been directly linked to SLE pathogenesis; however, few studies have shown an indirect link to SLE. For example, microRNA-125a has been shown to negatively regulate RANTES expression by targeting KLF13 in activated T cells. Zhao et al. showed that the expression of miR-125a was reduced, and the expression of its predicted target (KLF13) was increased in SLE patients. In another study, miR-125a levels were upregulated in the serum sample of lupus patients and were positively associated with the production of several inflammatory cytokines[46]. A recent genome-wide association study on autoimmune Addison's disease identified association peaks in one of the risk loci that harbor mir-125a. Our mechanism by which KLF13 promotes SLE pathogenesis is still limited since our study is focused on T cells and APCs. We cannot exclude the possibility that KLF13 may be affecting additional cell types, such as B cells, neutrophils, NK, and regulatory T cells, that could contribute to lupus pathogenesis. One intriguing finding in our analysis of published single-cell datasets was the strikingly high expression of *Klf13* gene in the plasmablasts in the kidney biopsies from lupus nephritis patients. We, therefore, predict that KLF13 might play a key role in generating autoantibodies and modulating the B cell function in autoimmunity. In the follow-up studies, it will also be essential to study the impact of the knockdown of KLF13 in a cell type-specific manner and other lupus-prone mouse models. Given our extensive molecular and phenotypic studies revealing *Klf13*$^{-/-}$ as a critical gene in lupus pathogenesis in mice and strikingly high expression of KLF13 in kidneys of lupus nephritis patients in the single cell datasets, it is essential to study the in-depth mechanisms by which KLF13 promotes lupus pathogenesis in SLE patients.

In summary, we identify *Klf13* as a lupus susceptibility gene within the *Sle3* interval that promotes SLE pathogenesis when combined with the *Sle1* locus. Upregulation of KLF13 causes enhanced production of RANTES, a chemokine that plays a critical role in lupus nephritis—one of the most severe clinical manifestations of SLE affecting 30% to 60% of adults and 70% of children with lupus[47]. We demonstrate that KLF13 mediates lupus nephritis by (1) eliciting the production of multiple inflammatory cytokines such as IL-2, IFNγ and RANTES in CD4 T cells as well as CCL2, TNFα, IL1β in BMDMs and BMDCs (2) modifying genome-wide transcription and chromatin structure of proinflammatory genes thereby resulting in hyperstimulation of innate and adaptive immune cell subsets (3) inducing chemokine RANTES which in turn results in the recruitment of inflammatory cells in the kidneys-evidenced by increased RANTES in *Sle1Sle3k* Kidneys. Thus, we propose that the proinflammatory state mediated by KLF13, when

combined with a breach in self-tolerance by *Sle1* locus, results in the acceleration of autoimmune phenotypes by producing hyperactive self-reactive T cells and APCs that infiltrate the kidneys and enhance ANA and autoantibody levels to tissue-specific antigens thereby causing extensive tissue damage ultimately leading to fatal lupus nephritis in *Sle1Sle3k* mice. Our study reveals *Klf13* as the key gene mediating lupus pathogenesis by impacting innate and adaptive immune systems. It highlights the key role of KLF13 in regulating toll receptor signaling and myeloid cell function. Our study provides an important insight into the genetic interactions involved in SLE disease pathogenesis. Given that mir-125a has been implicated in human LN, we believe that results from our study highlight an important role of *Klf13*, a target of miR-125a, in human LN that needs further exploration. Our results showing increased expression of RANTES in the kidneys of *Sle1Sle3k* mice align with numerous studies that have shown increased expression of RANTES in the blood and urine of patients with active LN. Since our mouse model used in the study is spontaneous and mimics human lupus in several ways, we believe our results can provide not only insight into potential mechanisms and pathways underlying the pathogenesis of lupus nephritis but also help provide guidance in designing future studies related to human LN. Our results, combined with future studies understanding the mir-125a/KLF13/RANTES axis and the epigenetics, will help identify novel therapeutic targets and develop rational design of new therapeutics for LN. Given that mir-125a and RANTES have been implicated in other autoimmune diseases such as inflammatory bowel disease (IBD), Rheumatoid arthritis (RA), Type 1 diabetes (TID), and multiple sclerosis (MS), we believe that KLF13 is a potential key transcription factor in the pathogenesis of these diseases. Thus, our findings could have implications for the rational design of new therapies for SLE and other autoimmune/inflammatory diseases.

Our study has the following limitations: Although based on extensive genomic and functional studies, we have identified *Klf13* as a key lupus-susceptible gene, a direct knockdown of KLF13 in *Sle1.Sle3k* mice, in a cell type-specific manner, in the follow-up studies may reveal a deeper understanding of the role of KLF13 in SLE pathogenesis. Our mechanism by which KLF13 promotes SLE pathogenesis is still limited since our study is focused on T cells and APCs and has not explored the role of the *Klf13* gene in B cells, NK cells, and other immune cell types that could potentially be playing a role in driving SLE pathogenesis in our mouse model. Although our mouse model is spontaneous and resembles human lupus phenotypes, further studies are warranted to study the role of KLF13 in LN patients to translate our findings to human disease.

Methods

Mice

*C57BL/6 J (*B6*)*, NZM2410, NZB, and NZW mice were purchased from the Jackson Laboratory. All mice were bred and maintained in a specific pathogen-free colony at the University of Texas Southwestern Medical Center and all animal experiments were carried out in accordance with IACUC approved animal protocols. Different truncated recombinant strains of *Sle3* were generated by backcrossing of *Sle3* mice to B6 assisted with microsatellite markers. Spleens and femurs from wild-type and *Klf13*$^{-/-}$ mice were received from Dr. Carol Clayberger (Northwestern University). 8–12-week-old mice were used for all studies involving CD4 T cells, BMDMs and BMDCs. All aging studies utilized 6–7 month or 9–12-month-old mice.

Renal assessment and autoantibody analysis

For renal assessment studies, mice were transferred into metabolic cages with a constant water source, and serum and urine were collected at 24 h. Urinary protein concentration was determined using the Coommassie® Plus Protein Assay kit (Pierce Biotechnology Inc. Rockford, IL). Blood urea nitrogen (BUN) was measured using the QuantiChrom Urea Assay Kit (BioAssay Systems, CA). Proteinuria was measured uing Albustix (SIEMENS, Germany). For anti-GBM studies, the protocol was followed exactly as described by Liu et al. 2009[18]. Kidneys were analyzed in a blinded manner, and the severity of GN was graded on a (0–4) scale using the guidelines set by the World Health Organization and criteria as described by Xie et al. 2013[48]. Serum samples were analyzed using anti-histone-DNA antibody Elisa as described by Mohan et al. 1999[16] and using custom autoantigen arrays developed at the UT Southwestern Microarray Core facility. Autoantigen array is a custom protein array panel of 96 antigens, including nuclear antigens, cytosolic/matrix antigens, and tissue/organ-specific antigens. It is a high throughput fluorescence-based detection system capable of simultaneously assaying antibody reactivity to 96 antigens with 5 ul of sera. Analysis of Autoantigen array data included the following pre-processing steps: (1) background subtraction and averaging of duplicated spots, (2) normalization of the signal intensity of each Ag using internal controls across all samples, and (3) normalized signal intensity (NFI) for each Ag (Ab) completed for each Genepix Report file generated per sample.

Cell Isolation, Elisa and Flow cytometry

Naive T cells were purified from splenic cell suspensions using EasySep mouse naive CD4 + T Cell Isolation Kit (StemCell Technologies) and cultured with or without anti-CD3 and anti-CD28 antibodies for different time points. Single-cell suspensions of Bone marrow were cultured with macrophage colony-stimulating factor (M-CSF) to generate BMDMs, or interleukin-4 (IL-4) plus granulocyte-macrophage-CSF (GM-CSF) to generate BMDCs (10 ng/ml for all cytokines; R&D Systems). All cells were cultured in RPMI-1640 with 10% FBS, 2 mM L-glutamine, 10 mM HEPES, 1 mM sodium pyruvate, 100 U/ml penicillin, 100 μg/mL streptomycin at 37 °C in a humidified CO_2 incubator and used for flow cytometry, RNA isolation, protein isolation, and functional assays. BMDMs or BMDCs were stimulated with 1 ug/ml R848 or 1 μM ODN18206 or 10 ng/ml of LPS for all the experiments. Cytokines CCL5, CCL2, IL-2, IFN- γ, IL-1β, IL-6, and TNF-α were measured using commercial ELISA kits (R&D Systems). All antibodies used were obtained from BD Biosciences, Pharmingen, or Upstate Laboratories and used at recommended dilutions. Cell staining was done by incubating cells with antibodies for 30 min on ice and washing twice with PBS. Data acquisition was done on LSR II (BD Biosciences) and analyzed using FlowJo software (FlowJo, LLC, Ashland, Oregon).

Immunohistochemistry staining and Western blot analysis

To detect the inflammatory cell infiltration, kidney tissues from B6, *Sle1*, and *Sle1Sle3k* were cut at 4 μm and mounted onto poly-L-lysine coated glass slides. After dewaxing and rehydration, sections were treated with 3% hydrogen peroxide in methanol for 10 min to block endogenous peroxidase activity before antigen retrieval by standard microwave-based methods in citrate buffer. The sections were incubated with antibodies to CD3 (CD3, Cat. no. MCA1477, 1:400; AbD Serotec, Raleigh, NC) and RANTES (Cat. no AAM49, 1:50; AbD Serotec, Raleigh, NC). Immunohistochemistry (IHC) was performed using EXPOSE rabbit and mouse-specific IHC kit (Abcam Inc, Cambridge, MA). Finally, a light hematoxylin counterstain was applied to each section. For western blot analysis, cells were lysed using RIPA lysis and extraction buffer (ThermoFisher) containing Thermo Scientific Pierce protease inhibitor minitablets. SDS-PAGE was used to resolve proteins and membranes were probed with the following antibodies: KLF13 (RFLAT-1) (Santa Cruz Biotechnology), GAPDH (Cell Signaling), and alpha-Tubulin (Cell Signaling). Proteins were detected using SuperSignal West Pico Chemiluminescent substrate (Pierce).

Whole genome sequencing, Sequence Alignment, Variant Calling, and Annotation

Genomic DNA was isolated from tail DNA using the in-house protocol. The DNA (2 μg) was sheared with an S220 Ultrasonicator (Covaris, Woburn, Massachusetts) and subsequently prepared using a KAPA LTP library preparation kit (KAPA Biosystems, Wilmington, MA 01887). After hybrid capture, amplification, and quality assessment, the samples were sequenced on Illumina NextSeq 500 using a standard 150-bp or HiSeq 2000 using a 100-bp paired-end protocol. Using default settings, the image analysis and base calling were performed with an Illumina pipeline. Sequence reads were

aligned to B6 mouse genome reference consortium mouse build 38 (release GRCm38/mm10, Dec. 2011) with the Burrows-Wheeler Aligner (BWA) version 0.6.1-r104. A Genome Analysis Toolkit (GATK) version v1.0.577[49] was used for base quality score recalibration, INDEL realignment, and duplicate removal. SNP and INDEL discovery and genotyping were performed simultaneously using variant quality recalibration according to GATK Best Practices recommendations[50,51]. All the variations were annotated, and their effects on genes were predicted using variant annotation and effect prediction tool SnpEff 3.0a or Variant Effect Predictor[52,53]. Genomic alignment and variant calling were performed using CLC Biosystems Genomic Workbench software (CLC Bio, a Qiagen company. Location: Waltham, MA). The data was further analyzed using Golden Helix software, Golden Helix Inc. Bozeman, MT.

RNA-Seq and real-time PCR analysis

RNA was isolated from CD4 T cells, BMDMs, and BMDCs using TRIzol reagent (Life Technologies) and RNAeasy kit per the manufacturer's protocol (Qiagen Corp. Valencia, CA). RNA quality was verified using Agilent Bioanalyzer 2100 (Agilent Technologies). One μg of total RNA was used to perform RNA-SEQ using TruSeq RNA Sample Preparation kit v2 (Illumina) as per the manufacturer's instructions. The library from each sample was sequenced on GAIIx sequencer or Illumina Hiseq 2000 or NextSeq 550 using 50-bp or 36-bp single-end protocol. Reads with phred quality scores less than 20 and less than 35 bp after trimming were removed from further analysis using trimgalore version 0.4.1. Quality-filtered reads were then aligned to the mouse reference genome GRCm38 (mm10) using the HISAT (v 2.0.1)[54] aligner using default settings and marked duplicates using Sambamba version 0.6.6[55]. Aligned reads were quantified using 'featurecount' (v1.4.6)[56] per gene ID against mouse Gencode version 20[57]. Differential gene expression analysis was done using the R package DEseq2 (v 1.6.3)[58]. Cutoff values of absolute fold change greater than 1.0 and FDR ≤ 0.05 were then used to select differentially expressed genes between sample group comparisons. GO enrichment and pathway analysis were performed using PANTHER to determine molecular and biological functional categories[59]. RNA-seq data for pathway and functional analysis was also analyzed using QIAGEN's Ingenuity® Pathway Analysis (IPA®, QIAGEN Redwood City, www.qiagen.com/ingenuity). RNA-seq data was also analyzed using CLC Biosystems Genomic Workbench software (CLC Bio, a Qiagen company. Location: Waltham, MA). *Klf13* gene expression was further validated by quantitative Real Time PCR analysis using TaqMan gene expression assays (Applied Biosystems): Mm00727486_s1 for *Klf13* and Mm03928990_g1 for Rn18s (18S ribosomal RNA) or *GAPDH to* be used s an internal control. Data analysis was performed using the comparative CT (ΔΔCT) method.

ATAC-sequencing

ATAC-seq library preparations were performed as described in Buenostro et al., 2015[60]. Briefly, 40,000-60,000 cells were used with 10 cycles of PCR amplification. All the libraries were sequenced using NextSeq 550 using 75-bp paired-end protocol. Reads were mapped to the B6 mouse reference genome mm9 or mm10 using BWA (Burrows-Wheeler transformation) Version: 0.7.9a-r786. Paired-end reads were adapter and quality trimmed using Trim Galore, then mapped to the mouse genome (GRCm38) using bwa. Duplicates were marked with picard, and alignments from replicates were merged; duplicates were remarked and proceeded with filtering to remove: reads mapping to mitochondrial DNA, mapping to blacklisted regions, reads marked as duplicates, secondary alignment reads, unmapped reads, multimapping reads, reads containing greater than 4 mismatches, soft-clipped reads, reads with a calculated insert size over 2 kb, read pairs mapping to a different chromosome, reads not in the FR orientation, reads where only one read of a pair fails any of the previous filters. Broad peaks were called with MACS2, peaks were annotated relative to gene features using HOMER, and consensus peaks across replicates were detected. Bam files were merged together from two independent ATAC-seq experiments and all Bedgraphs were converted to Bigwig files using galaxy browser tool Wig/Bedgraph-to-bigWig converter (Galaxy version 1.1.1). All samples were then visualized using Integrated Genomics Viewer (IGV) browser.

Statistics and reproducibility

Results are shown as mean ± SEM. Statistical significance was calculated using GraphPad Prism Software (GraphPad Software Inc, La Jolla, CA, USA) with Student's *t*-test, Wech's *t*-test, and Students 1-way parametric ANOVA comparison. RNA-seq data analysis is described in the RNA-seq section in Methods. For flow cytometry experiments, anti-nuclear autoantibodies (IgG) Elisa, anti-GBM challenge experiment, splenic weight, proteinuria, serum levels of BUN, autoantigen experiment, and immunohistochemistry, each replicate shown represents an independent single mouse. Real time PCR data analysis was performed using the comparative CT (ΔΔCT) method using three biological replicates. Unless specified in figure legends, all experiments were performed using atleast two biological replicates. Significance was considered at $^{*}p < 0.05$, $^{**}p < 0.01$, $^{***}p < 0.001$, $^{****}p < 0.0001$; ns = not significant.

Inclusion and ethics

We have complied with all relevant ethical regulations involoving the use of research animals in this study. All mice were bred and maintained in a specific pathogen-free colony at the University of Texas Southwestern Medical Center and all animal experiments were carried out in accordance with the Institutional Animal Care and Use Committee (IACUC) approved animal protocols

Data availability

All data generated in this study are included in Supplementary informaton. The data files behind all the graphs are included in the Supplementary Data file 1. The flow cytometry gating strategy and original uncropped western blots are provided in the Supplementary Fig. 1 and 2. All RNA-seq and ATAC-seq data are deposited to GEO (GEO accession: GSE278051) and whole genomic sequencing data is deposited to SRA (Bioproject: PRJNA1108703). All other data are available from the corresponding author on reasonable request.

Received: 28 July 2023; Accepted: 18 October 2024;
Published online: 06 November 2024

References

1. Arbuckle, M. R. et al. Development of autoantibodies before the clinical onset of systemic lupus erythematosus. *N. Engl. J. Med.* **349**, 1526–1533 (2003).
2. Feldman, C. H. et al. Epidemiology and sociodemographics of systemic lupus erythematosus and lupus nephritis among US adults with Medicaid coverage, 2000-2004. *Arthritis rheumatism* **65**, 753–763 (2013).
3. Mohan, C. & Putterman, C. Genetics and pathogenesis of systemic lupus erythematosus and lupus nephritis. *Nat. Rev. Nephrol.* **11**, 329–341 (2015).
4. Graham, R. R. et al. Genetic variants near TNFAIP3 on 6q23 are associated with systemic lupus erythematosus. *Nat. Genet.* **40**, 1059–1061 (2008).
5. Han, J. W. et al. Genome-wide association study in a Chinese Han population identifies nine new susceptibility loci for systemic lupus erythematosus. *Nat. Genet.* **41**, 1234–1237 (2009).
6. International Consortium for Systemic Lupus Erythematosus, G., Harley, J. B. et al. Genome-wide association scan in women with systemic lupus erythematosus identifies susceptibility variants in ITGAM, PXK, KIAA1542 and other loci. *Nat. Genet.* **40**, 204–210 (2008).
7. Rai, E. & Wakeland, E. K. Genetic predisposition to autoimmunity-what have we learned? *Semin. Immunol.* **23**, 67–83 (2011).

8. Raj, P. et al. Regulatory polymorphisms modulate the expression of HLA class II molecules and promote autoimmunity. *eLife* **5**, e12089 (2016).
9. Langefeld, C. D. et al. Transancestral mapping and genetic load in systemic lupus erythematosus. *Nat. Commun.* **8**, 1–18 (2017).
10. Kwon, Y. C., Chun, S., Kim, K. & Mak, A. Update on the genetics of systemic lupus erythematosus: genome-wide association studies and beyond. *Cells* **8**, 1180 (2019).
11. Wang, Y. F. et al. Identification of 38 novel loci for systemic lupus erythematosus and genetic heterogeneity between ancestral groups. *Nat. Commun.* **12**, 1–13 (2021).
12. Morel, L. Genetics of SLE: evidence from mouse models. *Nat. Rev. Rheumatol.* **6**, 348–357 (2010).
13. Morel, L., Rudofsky, U. H., Longmate, J. A., Schiffenbauer, J. & Wakeland, E. K. Polygenic control of susceptibility to murine systemic lupus erythematosus. *Immunity* **1**, 219–229 (1994).
14. Morel, L. et al. Functional dissection of systemic lupus erythematosus using congenic mouse strains. *J. Immunol.* **158**, 6019–6028 (1997).
15. Mohan, C., Alas, E., Morel, L., Yang, P. & Wakeland, E. K. Genetic dissection of SLE pathogenesis. Sle1 on murine chromosome 1 leads to a selective loss of tolerance to H2A/H2B/DNA subnucleosomes. *J. Clin. Investig.* **101**, 1362–1372 (1998).
16. Liu, K. et al. Sle3 and Sle5 can independently couple with Sle1 to mediate severe lupus nephritis. *Genes Immun.* **8**, 634–645 (2007).
17. Mohan, C. et al. Genetic dissection of lupus pathogenesis: a recipe for nephrophilic autoantibodies. *J. Clin. Invest*. **103**, 1685–1695 (1999).
18. Liu, K. et al. Kallikrein genes are associated with lupus and glomerular basement membrane-specific antibody-induced nephritis in mice and humans. *J. Clin. Investig.* **119**, 911–923 (2009).
19. Sobel, E. S. et al. Genetic dissection of systemic lupus erythematosus pathogenesis: evidence for functional expression of Sle3/5 by non-T cells. *J. Immunol.* **169**, 4025–4032 (2002).
20. Zhu, J. et al. T cell hyperactivity in lupus as a consequence of hyperstimulatory antigen-presenting cells. *J. Clin. Investig.* **115**, 1869–1878 (2005).
21. Mohan, C., Yu, Y., Morel, L., Yang, P. & Wakeland, E. K. Genetic dissection of Sle pathogenesis: Sle3 on murine chromosome 7 impacts T cell activation, differentiation, and cell death. *J. Immunol.* **162**, 6492–6502 (1999).
22. Okamoto, A., Fujio, K., Tsuno, N. H., Takahashi, K. & Yamamoto, K. Kidney-infiltrating CD4+ T-cell clones promote nephritis in lupus-prone mice. *Kidney Int.* **82**, 969–979 (2012).
23. Reddy, V., Jayne, D., Close, D. & Isenberg, D. B-cell depletion in SLE: clinical and trial experience with rituximab and ocrelizumab and implications for study design. *Arthritis Res. Ther.* **15**, S2 (2013).
24. Barber, D. F. et al. PI3Kgamma inhibition blocks glomerulonephritis and extends lifespan in a mouse model of systemic lupus. *Nat. Med.* **11**, 933–935 (2005).
25. Kyttaris, V. C., Wang, Y., Juang, Y. T., Weinstein, A. & Tsokos, G. C. Increased levels of NF-ATc2 differentially regulate CD154 and IL-2 genes in T cells from patients with systemic lupus erythematosus. *J. Immunol.* **178**, 1960–1966 (2007).
26. Liossis, S. N., Ding, X. Z., Dennis, G. J. & Tsokos, G. C. Altered pattern of TCR/CD3-mediated protein-tyrosyl phosphorylation in T cells from patients with systemic lupus erythematosus. Deficient expression of the T cell receptor zeta chain. *J. Clin. Investig.* **101**, 1448–1457 (1998).
27. Mak, A. & Kow, N. Y. The pathology of T cells in systemic lupus erythematosus. *J. Immunol. Res*. **2014**, 419029 (2014).
28. Fairhurst, A. M. et al. Yaa autoimmune phenotypes are conferred by overexpression of TLR7. *Eur. J. Immunol.* **38**, 1971–1978 (2008).
29. Liu, B. et al. TLR4 up-regulation at protein or gene level is pathogenic for lupus-like autoimmune disease. *J. Immunol.* **177**, 6880–6888 (2006).
30. Nickerson, K. M. et al. TLR9 regulates TLR7- and MyD88-dependent autoantibody production and disease in a murine model of lupus. *J. Immunol.* **184**, 1840–1848 (2010).
31. Huang, X., Dorta-Estremera, S., Yao, Y., Shen, N. & Cao, W. Predominant Role of Plasmacytoid Dendritic Cells in Stimulating Systemic Autoimmunity. *Front. Immunol.* **6**, 526 (2015).
32. Nie, J., Li, Y. Y., Zheng, S. G., Tsun, A. & Li, B. FOXP3(+) Treg Cells and Gender Bias in Autoimmune Diseases. *Front. Immunol.* **6**, 493 (2015).
33. Rowland, S. L. et al. Early, transient depletion of plasmacytoid dendritic cells ameliorates autoimmunity in a lupus model. *J. Exp. Med.* **211**, 1977–1991 (2014).
34. Shlomchik, M. J. Sites and stages of autoreactive B cell activation and regulation. *Immunity* **28**, 18–28 (2008).
35. Santiago-Raber, M. L. et al. Type-I interferon receptor deficiency reduces lupus-like disease in NZB mice. *J. Exp. Med.* **197**, 777–788 (2003).
36. Gordon, A. R. et al. Splenomegaly and modified erythropoiesis in KLF13-/- mice. *J. Biol. Chem.* **283**, 11897–11904 (2008).
37. Outram, S. V. et al. KLF13 influences multiple stages of both B and T cell development. *Cell cycle* **7**, 2047–2055 (2008).
38. Huang, B., Ahn, Y. T., McPherson, L., Clayberger, C. & Krensky, A. M. Interaction of PRP4 with Kruppel-like factor 13 regulates CCL5 transcription. *J. Immunol.* **178**, 7081–7087 (2007).
39. Kwon, S. J. et al. KLF13 cooperates with c-Maf to regulate IL-4 expression in CD4+ T cells. *J. Immunol.* **192**, 5703–5709 (2014).
40. Nikolcheva, T. et al. A translational rheostat for RFLAT-1 regulates RANTES expression in T lymphocytes. *J. Clin. Investig.* **110**, 119–126 (2002).
41. Song, A., Chen, Y. F., Thamatrakoln, K., Storm, T. A. & Krensky, A. M. RFLAT-1: a new zinc finger transcription factor that activates RANTES gene expression in T lymphocytes. *Immunity* **10**, 93–103 (1999).
42. Zhao, X. et al. MicroRNA-125a contributes to elevated inflammatory chemokine RANTES levels via targeting KLF13 in systemic lupus erythematosus. *Arthritis rheumatism* **62**, 3425–3435 (2010).
43. Arazi, A. et al. Accelerating Medicines Partnership in SLE network. The immune cell landscape in kidneys of patients with lupus nephritis. *Nat. Immunol.* **20**, 902–914 (2019).
44. Banerjee, S. et al. miR-125a-5p regulates differential activation of macrophages and inflammation. *J. Biol. Chem.* **288**, 35428–35436 (2013).
45. Mouri, K. et al. Prioritization of autoimmune disease-associated genetic variants that perturb regulatory element activity in T cells. *Nat. Genet* **54**, 603–612 (2022).
46. Eissa, E., Morcos, B., Abdelkawy, R. F. M., Ahmed, H. H. & Kholoussi, N. M. Association of microRNA-125a with the clinical features, disease activity and inflammatory cytokines of juvenile-onset lupus patients. *Lupus* **30**, 1180–1187 (2021).
47. Owen, K. A., Grammer, A. C. & Lipsky, P. E. Deconvoluting the heterogeneity of SLE: The contribution of ancestry. *J. Allergy Clin. Immunol.* **149**, 12–23 (2022).
48. Xie, C. et al. Lupus-prone strains vary in susceptibility to antibody-mediated end organ disease. *Genes Immun.* **14**, 170–178 (2013).
49. McKenna, A. et al. The Genome Analysis Toolkit: a MapReduce framework for analyzing next-generation DNA sequencing data. *Genome Res.* **20**, 1297–1303 (2010).
50. DePristo, M. A. et al. A framework for variation discovery and genotyping using next-generation DNA sequencing data. *Nat Genet.* **43**, 491–498 (2011).
51. Van der Auwera, G. A. et al. From FastQ data to high confidence variant calls: the Genome Analysis Toolkit best practices pipeline. *Curr Protoc Bioinformatics.* **43**, 11–10 (2013).
52. Cingolani, P. et al. A program for annotating and predicting the effects of single nucleotide polymorphisms, SnpEff: SNPs in the genome of Drosophila melanogaster strain w1118; iso-2; iso-3. *Fly (Austin)* **6**, 80–92 (2012).
53. McLaren, W. et al. The Ensembl Variant Effect Predictor. *Genome Biol.* **17**, 122 (2016).
54. Kim, D., Langmead, B. & Salzberg, S. L. HISAT: a fast spliced aligner with low memory requirements. *Nat Methods.* **12**, 357–360 (2015).

55. Tarasov, A., Vilella, A. J., Cuppen, E., Nijman, I. J. & Prins, P. Sambamba: fast processing of NGS alignment formats. *Bioinformatics.* **31**, 2032–2034 (2015).
56. Liao, Y., Smyth, G. K. & Shi, W. FeatureCounts: an efficient general purpose program for assigning sequence reads to genomic features. *Bioinformatics.* **30**, 923–930 (2014).
57. Frankish, A. et al. GENCODE reference annotation for the human and mouse genomes. *Nucleic Acids Res.* **47**, D766–D773 (2019).
58. Love, M. I., Huber, W. & Anders, S. Moderated estimation of fold change and dispersion for RNA-seq data with DESeq2. *Genome Biol.* **15**, 550 (2014).
59. Mi, H., Muruganujan, A., Casagrande, J. T. & Thomas, P. D. Large-scale gene function analysis with the PANTHER classification system. *Nat Protoc.* **8**, 1551–1566 (2013).
60. Buenrostro, J. D., Wu, B., Chang, H. Y. & Greenleaf, W. J. ATAC-seq: A Method for Assaying Chromatin Accessibility Genome-Wide. *Curr. Protoc. Mol. Biol.* **109**, 21–29 (2015).

Acknowledgements

We sincerely thank Jane Zheng for genotyping the mice and for technical help. We would also like to thank Genomics Core, Microarray Core, Mouse Breeding Core and Flow Core staff at UT Southwestern Medical center.

Author contributions

E.K.W., S.K., A.W., A.M.F., and K.L. conceptualized, designed and performed genetic dissection, flow cytometry and aging studies. E.K.W. and S.K. jointly supervised the work. S.K. conducted RNA-seq, ATAC-seq, genomics studies, and functional experiments. Q.L. and S.K. performed autoantigen array analysis. S.K., Y.D., and C.M. performed IHC staining. D.R. and S.K. performed a pathological assessment of the kidneys. C.C.[10] provided *Klf13* knock out mice. S.K., E.K.W., B.W., S.M., V.M., K.V., S.B., I.D., and C.A. performed bioinformatic data analysis. A.M., A.S., C.C.[1], and MI provided technical help with experiments. J.C. assisted with mouse breeding. S.K. drafted the manuscript.

Competing interests

The authors declare no competing interests.

Additional information

Supplementary information The online version contains supplementary material available at https://doi.org/10.1038/s42003-024-07099-0.

Correspondence and requests for materials should be addressed to Shaheen Khan.

Peer review information *Communications Biology* thanks Djamel Nehar-Belaid, Juliana Imgenberg-Kreuz and the other, anonymous, reviewer for their contribution to the peer review of this work. Primary Handling Editor: David Favero.